



Oxygen vacancy engineering of $\text{Bi}_2\text{O}_3/\text{Bi}_2\text{O}_2\text{CO}_3$ heterojunctions: Implications of the interfacial charge transfer, NO adsorption and removal



Yanfeng Lu^{a,b,c}, Yu Huang^{a,c,*}, Yufei Zhang^{a,c}, Jun-ji Cao^{a,c,*}, Haiwei Li^d, Cheng Bian^c, Shun Cheng Lee^d

^a State Key Lab of Loess and Quaternary Geology (SKLLQG), Institute of Earth Environment, Chinese Academy of Sciences, Xi'an, 710061, China

^b University of Chinese Academy of Sciences, Beijing, 100049, China

^c Key Laboratory of Aerosol Chemistry and Physics, Institute of Earth Environment, Chinese Academy of Sciences, Xi'an, 710061, China

^d Department of Civil and Environmental Engineering, The Hong Kong Polytechnic University, Hung Hom, Hong Kong

ARTICLE INFO

Keywords:

Oxygen vacancy
 $\text{Bi}_2\text{O}_3/\text{Bi}_2\text{O}_2\text{CO}_3$ heterojunction
 Photocatalysis
 Charge separation
 NO enrichment and removal

ABSTRACT

Efficient enrichment of targeted gaseous pollutants and fast diffusion rates of charge carriers are essential for the photocatalytic removal of nitric oxides at ambient concentration levels. Here we demonstrate that the construction of nano-structured $\text{Bi}_2\text{O}_3/\text{Bi}_2\text{O}_2\text{CO}_3$ heterojunctions with oxygen vacancies, increasing the photocatalytic NO removal activity, durability and selectivity for final products nitrate formation. Combining the experimental and density-functional theory calculations, it was elucidated that the presence of surface oxygen vacancies not only work as adsorption sites of low concentration NO, but also offer an intimate and integrated structure between surface defects and the light-harvesting heterojunctions, which can facilitate solar energy conversion and charge carrier transfer (more than 2 times). Control experiments with pristine $\text{Bi}_2\text{O}_3/\text{Bi}_2\text{O}_2\text{CO}_3$ also confirmed the crucial role of surface oxygen vacancies on the improvement of NO adsorption and removal ability during the photocatalytic degradation process. We explain the enhanced removal of NO through the synergistic effect of oxygen vacancy and heterojunction, which not only guaranteed the generation of more $\cdot\text{OH}$ radicals, but also provided another route to produce hydrogen peroxide. Our findings may provide an opportunity to develop a promising catalyst for air pollution control.

1. Introduction

Air pollution has become a highly concerned issue because of its close relationship with air quality and human health [1]. Nitric oxide (NO), as a typical air pollutant emitted by combustion processes, is one of the most important precursors for the formation of ozone and secondary organic aerosols (SOAs) through photochemical reactions [2]. Therefore, developing efficient and economical strategies to abate the atmospheric NO has become a global concern. Most of traditional methods suffer from low efficiency and high energy consumption [3]. Photocatalysis, a green chemistry technology using sunlight, performs excellently in decomposing air pollutants and has been attracting tremendous attention [4–6]. However, in view of the low concentrations of the gaseous pollutants in ambient atmosphere and the charge carrier diffusion restrictions of photocatalysts, the efficiency of NO removal and solar conversion are still not satisfactory, which restrains its practical application on air pollution control. Therefore, developing photocatalysts with high efficiency is crucial for practical air pollution

control.

Bismuth subcarbonate ($\text{Bi}_2\text{O}_2\text{CO}_3$) is a non-toxic and environment-friendly photocatalyst composed of alternate $\text{Bi}_2\text{O}_2^{2+}$ and CO_3^{2-} layers, of which the unique thin-layered structure can benefit the photo-induced separation and thus improve quantum yields [7]. Various $\text{Bi}_2\text{O}_2\text{CO}_3$ -based heterojunctions, including $\text{Bi}_2\text{O}_3/\text{Bi}_2\text{O}_2\text{CO}_3$ [8], $\text{Bi}_2\text{S}/\text{Bi}_2\text{O}_3/\text{Bi}_2\text{O}_2\text{CO}_3$ [9], $\text{Bi}_2\text{O}_3/\text{Bi}_2\text{O}_2\text{CO}_3/\text{Sr}_6\text{Bi}_2\text{O}_9$ [10], and $\text{Au}/\alpha\text{-Bi}_2\text{O}_3/\text{Bi}_2\text{O}_2\text{CO}_3$ [11] have been constructed to extend the optical absorption and improve the quantum yield of $\text{Bi}_2\text{O}_2\text{CO}_3$. Besides, the construction of electron-donating photocatalysts with well-designed activation center can offer an accessible kinetic pathway to improve the photocatalytic NO removal efficiency [12]. In particular, recent studies have revealed that some physical and chemical properties of metal oxides, such as light absorption and charge separation ability, can be modulated by their defect disorder [13]. The construction of oxygen vacancies on the surfaces of semiconductor photocatalyst can improve the visible light absorption, target air pollutants enrichment and electron mobility, which can eventually influence the reactivity of

* Corresponding authors at: State Key Lab of Loess and Quaternary Geology (SKLLQG), Institute of Earth Environment, Chinese Academy of Sciences, Xi'an, 710061, China.
 E-mail addresses: huangyu@iecas.cn (Y. Huang), cao@loess.llqg.ac.cn (J.-j. Cao).

photocatalysts [14,15].

Surface oxygen vacancies (OVs) have been considered as shallow donors for semiconductor photocatalysts and can serve as adsorption and reaction sites [16,17]. Recent studies on surface-OVs induced TiO_2 [18], Bi_2WO_6 [19], and $\text{Bi}_2\text{O}_2\text{CO}_3$ [20] nanostructures showed that the presence of OVs can significantly enhance their photocatalytic performance. For example, Li et al. investigated the effects of OVs for photocatalytic N_2 fixation by BiOBr nanosheets [16]. The OVs- BiOBr nanosheets were regarded as the catalytic centers capable of adsorbing and activating N_2 because their defect states can dynamically trap the directly excited electrons from the CB of BiOBr . Pipornpong et al. proved that the oxygen vacancy defect surface of TiO_2 showed the obvious chemisorption of CO_2 with spin-unpolarized [21]. The influence of oxygen vacancy about CO_2 adsorption on the $\beta\text{-Ga}_2\text{O}_3$ surface was also studied by the DFT calculations [22]. The results proved that a high oxygen vacancy density can provide active sites for adsorption and activation of CO_2 , improving the catalytic activity for CO_2 conversion. Moreover, Xie et al. found that OVs-induced ultrathin In_2O_3 porous sheets exhibited a narrowed band gap and higher charge carrier concentration compared with pristine In_2O_3 [23]. Dong et al. observed that defective $\text{Bi}_2\text{O}_2\text{CO}_3$ microspheres exhibit synergistic effect of thermocatalysis and photocatalysis due to the existence of oxygen defects, which can directly activate the adsorbed O_2 to generate the active species, depending on their abundant surface donors and adsorption geometry [13]. O_2 activation is an effective strategy in enhancing the catalytic performance during the photocatalytic reaction process. The formation of active species can subsequently initiate chemical reaction for air pollutants removal. For these OVs-induced materials, oxygen vacancies and the substrates work in a cooperative way to enhance the photocatalytic activity. Therefore, combining the merits of OVs and heterojunctions is a promising strategy to explore photocatalysts with high photocatalytic activity.

In this work, OVs-induced $\text{Bi}_2\text{O}_3/\text{Bi}_2\text{O}_2\text{CO}_3$ heterojunctions were controllably prepared via *in-situ* heat-treatment method under nitrogen atmosphere for the first time. Various characterization methods were adopted to investigate the formation and properties of OVs. The effect of OVs on the improvement of photocatalytic activity of $\text{Bi}_2\text{O}_3/\text{Bi}_2\text{O}_2\text{CO}_3$ was further discussed.

2. Experimental section

2.1. Preparation of OVs-induced $\text{Bi}_2\text{O}_3/\text{Bi}_2\text{O}_2\text{CO}_3$ heterojunctions (OV-BO/BOC)

All chemicals were of analytical grade and directly used without further purification. Firstly, $\text{Bi}_2\text{O}_2\text{CO}_3$ nanosheets (BOC) were synthesized by a hydrothermal method with $\text{BiC}_6\text{H}_5\text{O}_7$ as the precursor. In brief, 1 mmol $\text{BiC}_6\text{H}_5\text{O}_7$ was dissolved in 15 mL of $\text{NH}_3\text{H}_2\text{O}$ solution. The mixture was transferred to a 20 mL Teflon-lined stainless steel autoclave and maintained at 180 °C for 24 h. Before drying at 60 °C, the BOC was collected by centrifugation and washed several times with deionized water. Secondly, the BOC sample was moved into a porcelain combustion boat at 350 °C for 2 h under nitrogen atmosphere at 1.2 L min⁻¹ to obtain OV-BO/BOC. For comparison, BO/BOC sample was prepared with heat treatment in air under other identical conditions. Moreover, the OV-BO/BOC sample was calcined at 250 °C for 2 h in the oxygen-enriched atmosphere to obtain R-BO/BOC.

2.2. Characterization methods

Powder X-ray diffraction (XRD) measurements were recorded on a Philips X'pert PRO SUPER diffractometer with Cu K α radiation ($\lambda = 0.15406$ nm). The morphologies of the materials were illustrated by a SUPRA 55 field emission scanning electron microscopy (SEM) and a JEOL JEM-2010 transmission electron microscopy (TEM). The Brunauer-Emmett-Teller (BET) surface area was measured by N₂

adsorption/desorption isotherms at 77 K by using a Micrometrics Gemini VII 2390 instrument. Elemental analyses were performed using an Elementarvario EL instrument with He purging for 20 s before test (detection limit: 0.015%, standard deviation: $\leq 0.1\%$ abs). The optical absorption of the samples was recorded on a Varian Cary 100 Scan UV-vis spectrophotometer using BaSO₄ as reference. Raman spectra were recorded by a Horiba JobinYvon HR800 using 532 nm of a YAG laser as the excitation source. Photoluminescence (PL) was performed with a HITACHI F-7000 to probe the charge separation property. The zeta potentials were measured by Malvern Zetasizer Nano ZS analyzer using an electrophoretic light scattering spectrophotometer. A Bruker ER200-SRC spectrometer was used to detect *in situ* electron spin resonance (ESR) signals of the samples at low temperature (130 K) and to detect free radicals by mixing the as-prepared samples with 25 mM of 5,5'-dimethyl-1-pyrroline-N-oxide (DMPO) solution. The light irradiation source was a PLS-SXE 300 W Xe arc lamp.

The temperature-programmed desorption (TPD) experiments were performed in a quartz reactor using a TCD as detector. The temperature-programmed desorption of O₂ (O₂-TPD) measurement using helium (He) gas was performed with 0.5 g samples. The pretreatment of raw sample was firstly applied in pure He with a flow rate of 40 mL min⁻¹ at 120 °C for 120 min. After cooled down to room temperature, O₂-TPD measurement was performed up to 600 °C at a heating rate of 5 °C min⁻¹ in the pure He atmosphere. The temperature-programmed desorption of NO (NO-TPD) experiments were performed with 0.5 g catalysts, which was dosed with 50 ppm NO for 30 min after pretreated with pure He. The catalysts were purged with pure He gas with a flow rate of 25 mL min⁻¹ for 90 min to remove gas-phase NO completely. Finally, NO-TPD was performed up to 600 °C at a heating rate of 8 °C min⁻¹ in the pure He atmosphere.

2.3. Theoretical calculations

The theoretical calculations in our study were performed with the density functional theory (DFT) provided by the program CASTEP package [24,25], which employed the plane-wave basis sets to treat valence electrons and norm-conserving pseudo-potentials to approximate the potential field. The supercell models of the bulk Bi_2O_3 and $\text{Bi}_2\text{O}_2\text{CO}_3$ were built, and the supercells of $1 \times 1 \times 2$ and $2 \times 1 \times 2$ were respectively used for Bi_2O_3 and $\text{Bi}_2\text{O}_2\text{CO}_3$. The crystal models of the $\text{Bi}_2\text{O}_3/\text{Bi}_2\text{O}_2\text{CO}_3$ heterojunction with the interfaces composed of Bi_2O_3 (001) and $\text{Bi}_2\text{O}_2\text{CO}_3$ (001) lattice planes were also constructed. The exchange-correlation functional was implemented by using the Perdew-Burke-Ernzerhof of (PBE) [26] to describe the exchange-correlation energy and electron interactions. The Brillouin zones were separately sampled at $3 \times 3 \times 4$, $3 \times 3 \times 3$ and $3 \times 3 \times 4$ Monkhorst-Pack k -points for the three models [27,28]. A plane-wave cutoff of 400 eV was used for all calculations. The energy and residual force convergence criterion were set to 2.0×10^{-6} eV/atom and 0.05 eV/Å for geometry optimization, respectively. A $3 \times 3 \times 1$ Monkhorst-pack k -point mesh was used to calculate the density of states (DOS) of the bulk Bi_2O_3 , $\text{Bi}_2\text{O}_2\text{CO}_3$ and $\text{Bi}_2\text{O}_3/\text{Bi}_2\text{O}_2\text{CO}_3$ heterojunction. Charge transfer was calculated by electron density difference (EDD) and the Mulliken Population Analysis (MPA) [28]. To calculate the oxygen vacancy formation energies (ΔE_{vac}) and NO adsorption energies (ΔE_{ad}) of Bi_2O_3 and $\text{Bi}_2\text{O}_2\text{CO}_3$, the slab models with (001) surfaces exposed respectively for Bi_2O_3 and $\text{Bi}_2\text{O}_2\text{CO}_3$ were built [20,29]. The ΔE_{vac} and ΔE_{ad} of NO were defined using the separate formulas (shown in Supporting Information).

3. Results and discussion

3.1. Theoretical predictions

Theoretical calculations based on density functional theory (DFT) were carried out to predict whether the presence of OVs was beneficial for NO adsorption and charge separation. As shown in Table S1, the

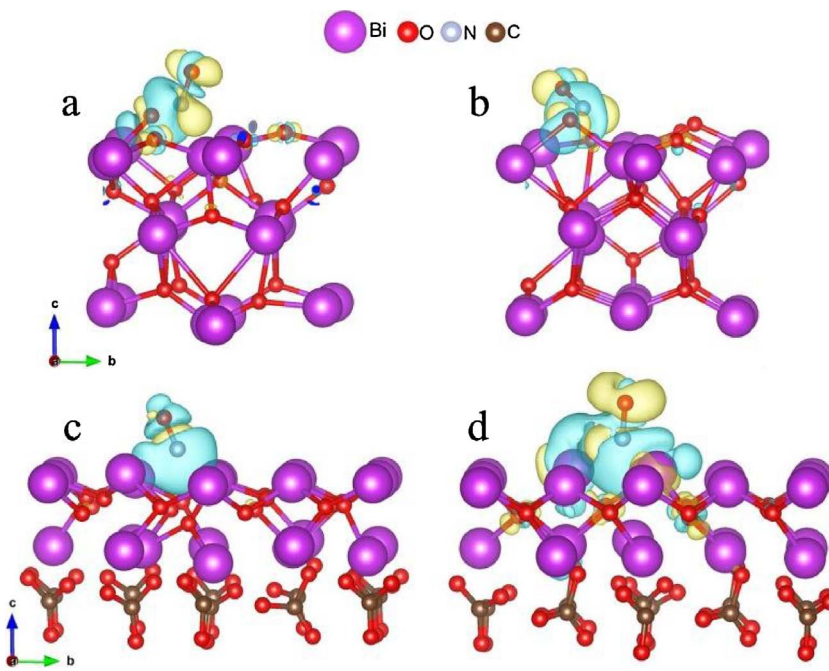


Fig. 1. Differential charge density distributions of the NO-adsorbed slab models of (a) (001) surface of Bi_2O_3 (side view), (b) Bi_2O_3 ($\text{Ov},_2$) (side view), (c) (001) surface of $\text{Bi}_2\text{O}_2\text{CO}_3$ (side view) and (d) $\text{Bi}_2\text{O}_2\text{CO}_3$ ($\text{Ov},_2$) (side view). The blue and yellow colors represent increase and decrease in electron density, respectively, revealed by DFT calculations. (For interpretation of the references to colour in this figure legend, the reader is referred to the web version of this article.)

average ΔE_{vac} on the (001) surface of Bi_2O_3 is lower than that on the (001) surface of $\text{Bi}_2\text{O}_2\text{CO}_3$, indicating that it is easier for Bi_2O_3 to form oxygen vacancies on the (001) surface of Bi_2O_3 [30]. The slab models with comparably smaller oxygen vacancy formation, i.e., $\text{Ov},_2$ for both Bi_2O_3 and $\text{Bi}_2\text{O}_2\text{CO}_3$, were chosen to further calculate the ΔE_{ad} of NO on their surfaces. The results of Table S2 show that the presence of oxygen vacancy benefits NO adsorption. It can also be seen in Fig. 1 that both Bi_2O_3 and $\text{Bi}_2\text{O}_2\text{CO}_3$ form stable NO chemisorption for the reason of the oxygen vacancy formation. The chemisorption of NO is accompanied by electron transfer from Bi_2O_3 or $\text{Bi}_2\text{O}_2\text{CO}_3$ sites to NO species. It is thus anticipated that the strong electron coupling between defective Bi_2O_3 or $\text{Bi}_2\text{O}_2\text{CO}_3$ sites and NO species would serve as a bridge to enable energy transfer from excitons to NO species once Bi_2O_3 or $\text{Bi}_2\text{O}_2\text{CO}_3$ or $\text{Bi}_2\text{O}_3/\text{Bi}_2\text{O}_2\text{CO}_3$ sites [16]. In particular, the NO on the surfaces of Bi_2O_3 slabs tend to form NO_2 -like structures with the bridge oxygen atoms, prompting the NO catalytic reaction. Furthermore, nitrogen and oxygen atoms on the surface of $\text{Bi}_2\text{O}_2\text{CO}_3$ slabs tend to form stable ionic or coordinate bonds with the bridge bismuth atoms, which is also beneficial for the NO adsorption.

3.2. Phase and morphology

For the synthesized BO/BOC and OV-BO/BOC samples, we found that the color of samples accompanied by the introduction of oxygen vacancies changed from yellow to dark-green (Fig. 2a). However, when the dark-green OV-BO/BOC was disposed in the oxygen-enriched atmosphere, the surface-OVs structure were repaired to obtain yellow powders. The crystalline phases of the as-synthesized samples were analyzed by XRD as shown in Fig. 2b. All peaks of BOC can be precisely indexed with pure BOC with an orthorhombic crystal structure (PCPDS No.84-1752). After the heat-treatment of BOC at 350 °C for 2 h in different atmosphere, a tetragonal Bi_2O_3 was appeared (JCPDS No.27-50). These results suggested that we successfully obtained BOC-based heterojunctions via an *in-situ* heat-treatment process. The crystal models of the BO/BOC heterojunction with the interfaces composed of BO (001) and BOC (001) lattice planes were also constructed as shown in Fig. 2c. It was found that phase transformation or any impurities were not observed among BO/BOC, OV-BO/BOC and R-BO/BOC. Using Scherrer Equation, $D = 0.9 \lambda/(B \cos \theta)$, where 0.9 is the typical value for the shape factor K, λ is the X-ray wavelength, B is the line

broadening full width at half maximum (FWHM) of peak height in radians, and θ is the Bragg diffraction angle, the average particle sizes of different samples were estimated through the diffraction peaks [31]. As shown in Table S3, the crystallite sizes are similar among the three samples. Moreover, the mass ratio of BO and BOC in the BOC-based heterostructure photocatalysts were determined by element analysis. As shown in Table S3, the variations of the mass ratio of BO and BOC in BO/BOC and OV-BO/BOC are ignorable (mass ratio: $\text{Bi}_2\text{O}_3 \sim 44\%$, $\text{Bi}_2\text{O}_2\text{CO}_3 \sim 56\%$).

Fig. 3a, d and g show the typical SEM images of the BOC, BO/BOC and OV-BO/BOC. The BOC sample is composed of numerous nanosheets (Fig. 3a). After heat-treatment at 350 °C, BO/BOC and OV-BO/BOC are still of nanosheet structures, but the surface become rough and surface porous structures are formed (Fig. 3b). As shown in Fig. 3b, e and h, the low-magnification TEM images are in good agreement with the SEM results. Moreover, the HRTEM images of BO/BOC and OV-BO/BOC demonstrate their detailed nano-junction structures shown in Fig. 3f and i. It clearly shows two different lattice images with *d*-spacing of ~0.38 and ~0.32 nm, which corresponds to the (002) lattice plane of BOC [9] and the (120) lattice plane of BO [8], suggesting that the BOC-based heterojunction structure can be successfully constructed. In addition, the elemental X-ray mapping of OV-BO/BOC (Fig. 3d-g) further illustrates that the elements of C, Bi and O are uniformly distributed.

The crystal lattice fringes of the samples were examined by HRTEM. Fig. 3a displays an interplanar spacing of about 0.38 nm, corresponding to the BOC (002) lattice plane [9]. The lattice fringes of BOC are very clear. However, the edge of OV-BO/BOC become dim and disordered (Fig. 4a). As shown in Fig. 4c and d, the edge of BOC and BO both are dim and disordered, illustrating the surface structures are damaged and the surface-OVs are probably formed [19]. In contrast, the lattice fringes of BO/BOC exhibit high crystalline nature and well-resolved lattice feature throughout the whole particles (Fig. S3). In addition, the selected area electron diffraction (SAED) pattern was performed to confirm the crystallinity of OV-BO/BOC (the inserts of Fig. 4c and d). They present a set of diffraction points from OV-BO/BOC, which can be indexed with an orthorhombic crystal structure from BOC and a tetragonal crystal structure from Bi_2O_3 .

XPS was performed to investigate the surface chemical composition and chemical states of samples. The survey spectra of the different samples show the presence of Bi, C, and O (Fig. S4a) [13]. Fig. S4b

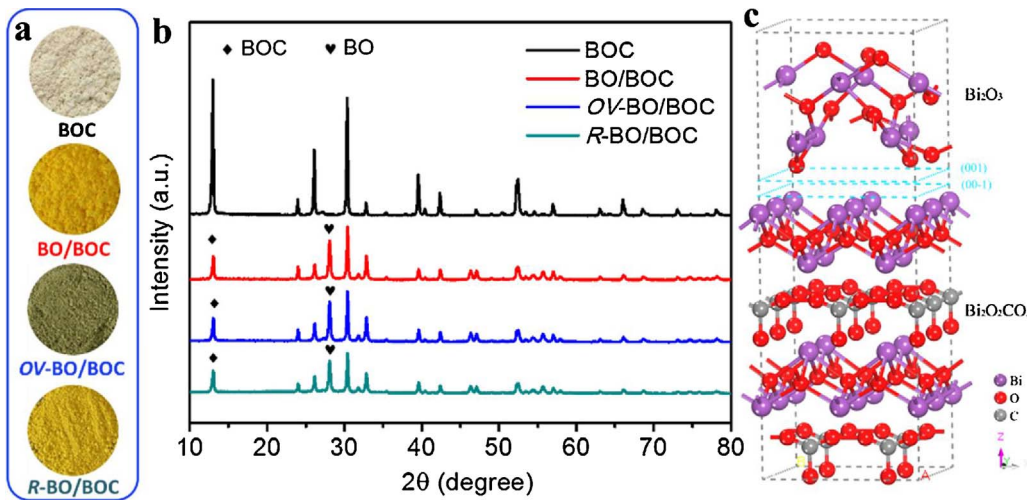


Fig. 2. (a) The powder samples showing different colors; (b) XRD patterns and the corresponding color of BOC, BO/BOC, OV-BO/BOC and R-BO/BOC; (c) The crystal models of BO/BOC heterojunction with the interfaces composed of BO (001) and BOC (001) lattice planes.

displays the high-resolution XPS spectra of Bi 4f orbitals for BO/BOC, OV-BO/BOC and R-BO/BOC. Two characteristic peaks of the oxidation state of Bi³⁺ in BO/BOC located at 163.9 and 158.6 eV, which are the indicative of Bi 4f_{5/2} and Bi 4f_{7/2}, respectively. After *in situ* pyrolysis reaction of BOC in nitrogen atmosphere, the Bi 4f_{5/2} and Bi 4f_{7/2} peaks of OV-BO/BOC are shifted up by 0.3 eV, while the peaks of R-BO/BOC almost return to original BO/BOC position. As reported elsewhere, it needs to compensate the charge balance in the as-prepared sample when oxygen vacancies are introduced [32,33]. Therefore, the above changes are ascribed to maintain the electrostatic balance for each oxygen vacancy generating. Besides, the peaks of O 1 s also show a same trend shown in Fig. S4c [20,34]. Consequently, the binding energies of both O and Bi atoms in three samples shift positively.

3.3. Formation of surface oxygen vacancies

O₂-TPD can be used to investigate the deoxidation process of the as-prepared samples [35]. As shown in Fig. S5, the O₂-TPD profile of BOC exhibits a sharp peak at about 413 °C, which can be ascribed to the transformation of BOC to Bi₂O₃ via the *in situ* pyrolysis reaction. Nevertheless, there are two various peaks at about 105 °C and 230 °C from the inset, which are inferred as the partial loss of oxygen atoms on BOC sample, resulting in the formation of surface-OVs [32]. Therefore, we infer several oxygen atoms are removed from the surfaces of BOC and Bi₂O₃, generating surface-OVs with different number and kind gradually [36].

Raman spectra was collected to characterize the effect of oxygen vacancies on the surface structure of the samples. As shown in Fig. 5a, stretching modes near 155 cm⁻¹ and 459 cm⁻¹ are generated by the Bi–O bond interaction [37]. Compared with those of BO/BOC and R-BO/BOC, the peak intensity near 155 cm⁻¹ and 459 cm⁻¹ for OV-BO/BOC is slightly reduced, while a weaken signal at 618 cm⁻¹ appears, due to the lattice expansion and mode softening induced by the presence of oxygen vacancy [38]. The broader or almost disappearance of stretching mode near 155 cm⁻¹ and 459 cm⁻¹ and partially overlapping with the band at 618 cm⁻¹ could be attributed to the broken trend and disordered of Bi–O coordination bond in Bi–O layers [39]. The results illustrate the presence of surface-OVs, which are consistent with the dim and disordered surface structure of HRTEM observations shown in Fig. 4.

ESR spectroscopy was further adopted to confirm the existence of oxygen vacancies. ESR test can not only detect any deficiency in a direct and sensitive way, but also can determine free radicals or other paramagnetic centers by the g-factor value produced under different conditions [13]. The g-factor value of free electron is g_e ~ 2.0023 [30]. Compared with the theoretical value, it has a little deviation in the

experiment results because the electron is not an isolate unit which is affected by the surrounding quantized electromagnetic field. As shown in Fig. 5b, the remarkable symmetric peaks at about g ~ 2.001 for OV-BO/BOC centered are observed, which are of typical peaks of oxygen vacancy [13,20]. Nevertheless, no ESR signals can be observed for BO/BOC sample. Once the oxygen vacancies are repaired after calcination in oxygen-enriched atmosphere, the signal for R-BO/BOC at g ~ 2.001 nearly disappeared. Based on the results from HRTEM, Raman spectra and ESR test, the surface oxygen vacancies are successfully induced on the Bi₂O₃/Bi₂O₂CO₃ heterojunction by an *in-situ* heat-treatment strategy.

3.4. Optical and gaseous NO adsorption property

The color of BO/BOC changed from yellow to dark-green (OV-BO/BOC) caused by the increasing oxygen vacancy, implying increased optical absorption ability in the visible light region. As shown in Fig. 5c, the absorption sharp edge of BOC sample is at 390 nm, while that of BO/BOC heterojunction appears red shift. The absorption intensity of OV-BO/BOC was enhanced in the visible light region and the absorption edges is around 500–800 nm, indicating the oxygen vacancies possessing a new donor level, which endow the semiconductors with the narrowed band gap energy to facilitate visible light harvesting [40]. After the repair of surface-OVs, the absorption band edge of R-BO/BOC can recover to the position of that of OV-BO/BOC. This phenomenon suggests that the introduction of surface-OVs on BO/BOC heterojunction can effectively tune its band gap energy and visible light absorption ability, which are crucial for the improvement of photocatalytic activity [41].

NO-TPD was conducted to investigate the relationship between the presence of surface-OVs and gaseous NO adsorption property [16]. Actually, NO adsorption on the surface of the catalyst is the first step during the photocatalytic reaction. The oxygen vacancies on the surface are regarded as the catalytic centers capable of adsorbing NO, and the NO conversion efficiency over OV-BO/BOC would be highly dependent on the presence of surface-OVs. As observed from the NO-TPD profiles shown in Fig. 5d, two distinct desorption peaks at around 120 °C and 215 °C are observed over the as-prepared BO/BOC, OV-BO/BOC and R-BO/BOC samples, corresponding to the physisorption and chemisorption modes of NO, respectively. Compared with BO/BOC and R-BO/BOC, the peak intensity at 215 °C is much more sensitive for OV-BO/BOC, indicating its strong adsorption ability of NO. The experimental results are well consistent with DFT calculation results regarding to NO adsorption energies (Table S2). In addition, the decrease of the zeta potential (BO/BOC: 15.6 mV; OV-BO/BOC: 13.2 mV, Table S3) is clearly observed due to the existence of surface-OVs [42]. Moreover,

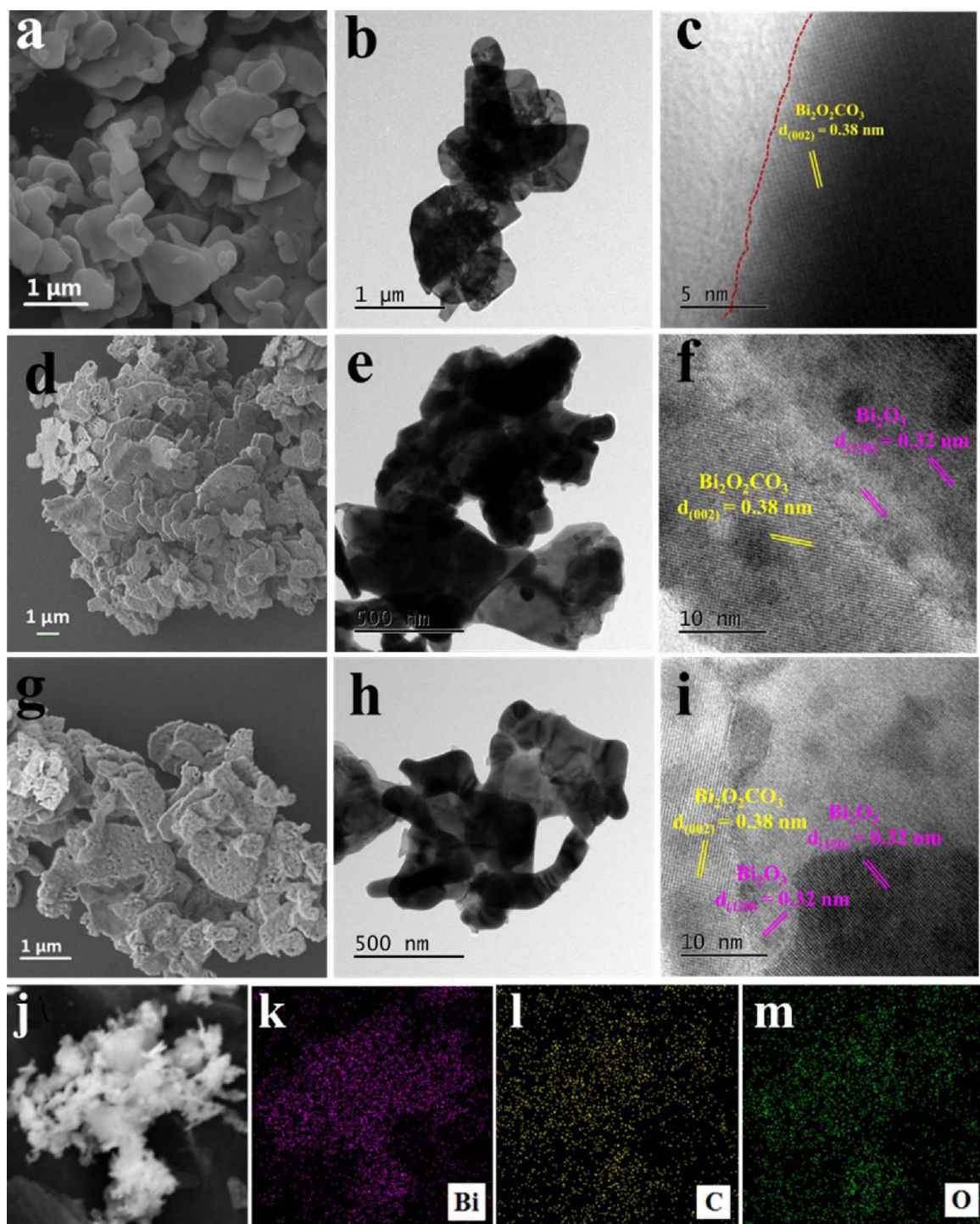


Fig. 3. SEM and TEM images of BOC (a, b, c), BO/BOC (d, e, f) and OV-BO/BOC (g, h, i); elemental distribution maps (j–m) for bismuth, carbon and oxygen of OV-BO/BOC heterojunction.

the BET surface area of OV-BO/BOC is similar to that of BO/BOC and the mass ratios of Bi₂O₃ to Bi₂O₂CO₃ are rarely changed (Table S3). These results indicate that the crucial role of surface-OVs on the improvement of NO adsorption ability, which can significantly facilitate the enrichment of target gas pollutants at ambient concentrations during the photocatalytic degradation process.

3.5. Evaluation of photocatalytic activity

The photocatalytic activities of the as-prepared samples were evaluated by the removal of NO at ppb levels in a continuous reactor [16].

As shown in Fig. 6a, the NO removal rates over BOC, BO/BOC, and OV-BO/BOC were 23%, 35% and 44% under simulated solar light irradiation, respectively. The photocatalytic activity of the repaired R-BO/BOC sample reached the same level with BO/BOC. That is, OV-BO/BOC exhibits the highest photocatalytic activity for the NO removal due to the existence of surface-OVs. Moreover, as shown in Fig. S6, the NO removal rate shows the similar trends under visible light and solar light irradiation.

After the photoactivity test, the accumulated amounts of NO₂[−] and NO₃[−] on the surfaces of the as-prepared samples were determined by ion chromatography (IC) method (the corresponding time scale IC

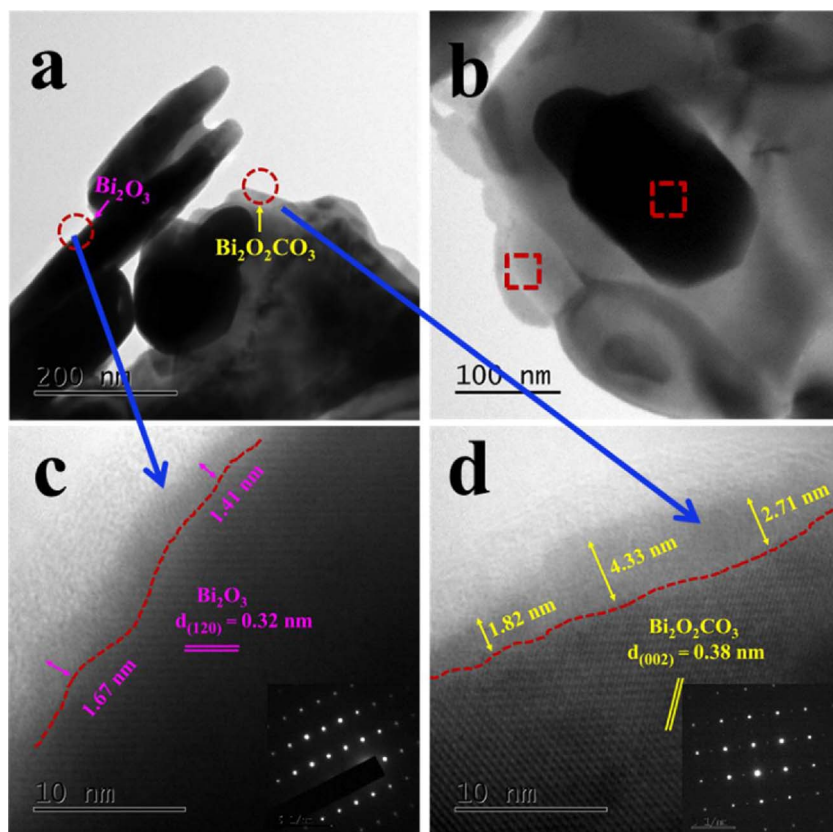


Fig. 4. Representative TEM (a, b) and HRTEM (c, d) images of the OV-BO/BOC with SAED patterns. The red dash lines in the HRTEM images display the boundary of crystalline and disordered layer. (For interpretation of the references to colour in this figure legend, the reader is referred to the web version of this article.)

profiles with the generation of NO_2^- and NO_3^- are shown in Fig. S7). The Fig. 6b shows that the amount of NO_3^- (899 $\mu\text{g/g}$) over OV-BO/BOC is the highest, according to a plot of the production amount of NO_2^- and NO_3^- . Besides, an unstable intermediate NO_2^- shows by just

one weak signal generated in the photocatalytic reaction of OV-BO/BOC. The phenomenon illustrates the most of NO is oxidized to NO_3^- . These results provide an accurate evidence of major NO transformation generated by OV-BO/BOC. However, large amount of NO_3^- ions

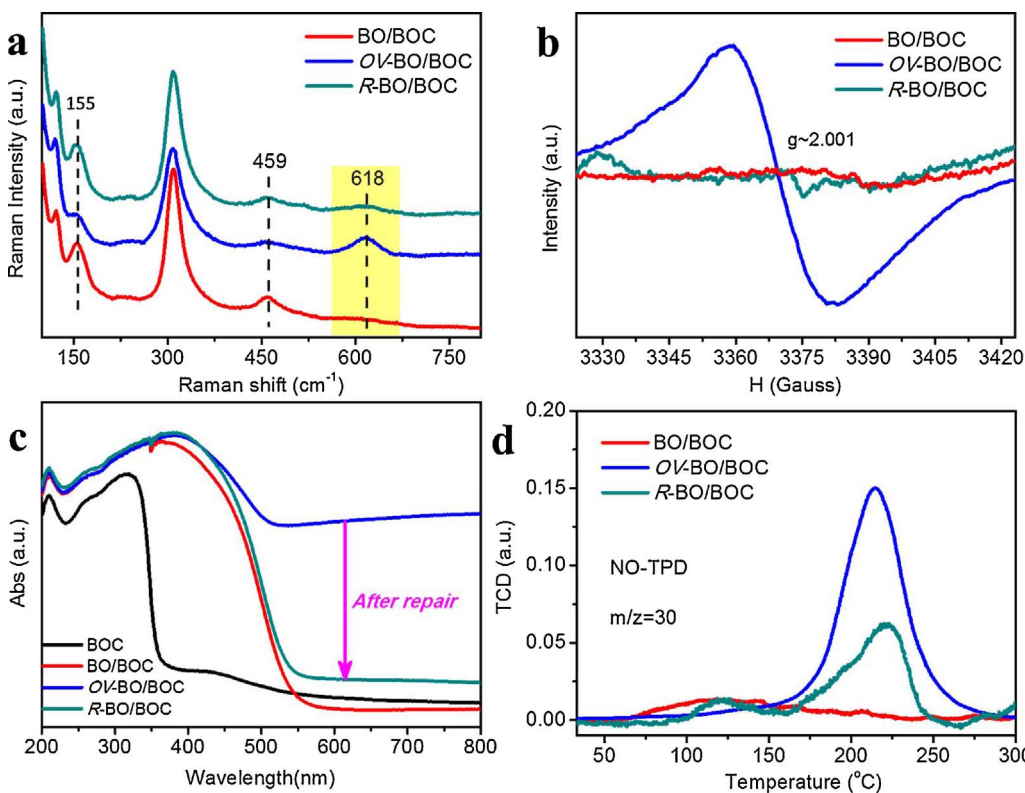


Fig. 5. (a) Raman spectra of samples using 514 nm excitation; (b) Situ ESR spectra of BO/BOC, OV-BO/BOC and R-BO/BOC; (c) UV-vis DRS of the as-prepared samples; (d) NO-TPD profiles of the BO/BOC, OV-BO/BOC and R-BO/BOC.

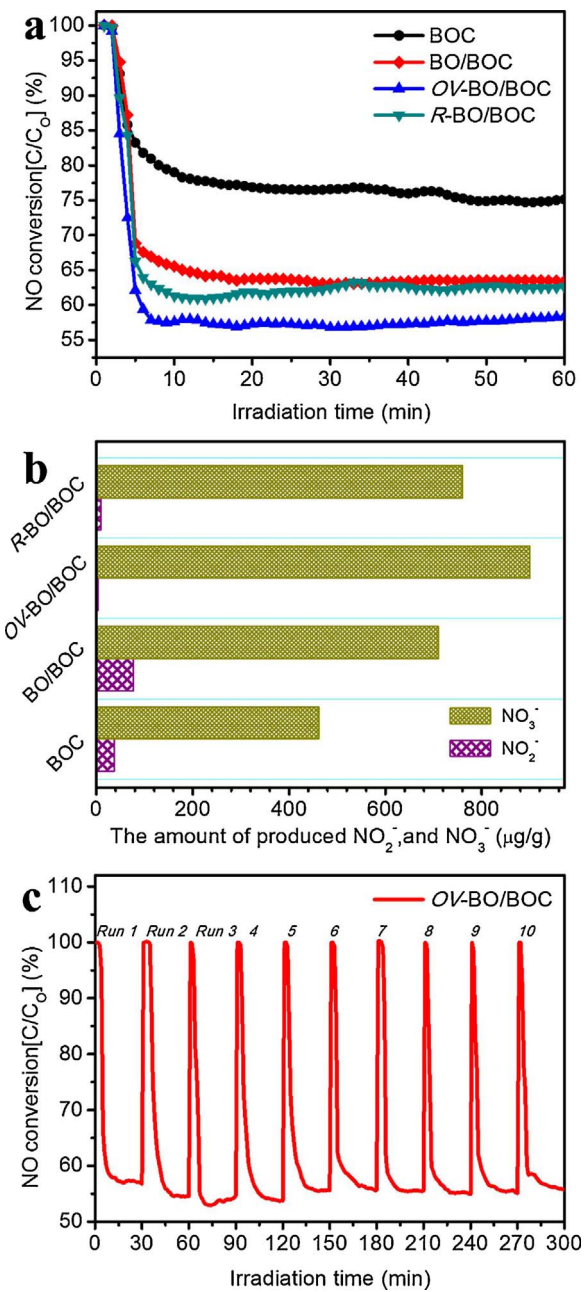


Fig. 6. (a) NO photocatalytic degradation under solar light irradiation, (b) amount of produced NO_2^- and NO_3^- for different samples and (c) photochemical stability of the OV-BO/BOC sample.

occupy the surface active sites and maybe can cause the deactivation of catalysis. In order to investigate the stability of catalyst, the cycle-tests of OV-BO/BOC were performed (Fig. 6c). In a ten-cycle test, the NO removal efficiency of the OV-BO/BOC is quite stable. Moreover, the stability of OV-BO/BOC was further confirmed via *in situ* ESR (Fig. S8). Compared with the sample before repeated irradiation, the ESR pattern of the sample after repeated irradiation only has slight loss but almost well-maintained the intensity, which suggests its oxygen vacancy structure stability. The result implies that the OV-BO/BOC can more oxidize NO to NO_3^- ion located at a different location (via a surface vacancy diffusion mechanism) [43], thus alleviating the deactivation to catalyst. It is inferred that the introduction of surface-OVs, as shallow donors for semiconductor photocatalysts, can serve as adsorption and reaction sites on the photocatalyst surface.

3.6. Charge separation efficiency, reactive species identification, and mechanism of photocatalytic NO removal over OV-BO/BOC

In order to investigate the effect of oxygen vacancy on the improvement of photocatalytic activity, photoelectrochemical tests and DFT calculation methods have been adopted to characterize the photogenerated charge separation efficiency. Moreover, the involved reactive oxygen species during the photocatalytic processes were also identified.

The separation efficiency of photo-generated electron-hole pairs plays an important role on the improvement of photocatalytic activity [44]. Firstly, the interfacial charge transport properties were investigated through electrochemical impedance spectroscopy (EIS). On the EIS plane, one arc indicates that the surface charge transfer experiences the rate-determining step in the photocatalytic reaction. The shorter the arc radius of EIS Nyquist plots track becomes, the smaller the charge transfer resistance is [18,44]. As shown in Fig. 7a, the radius of all the electrodes follows an order: OV-BO/BOC < R-BO/BOC < BO/BOC < BOC, indicating the OV-BO/BOC electrode exhibited the highest charge transfer rate. Meanwhile, Fig. 7b shows that the photocurrent density of OV-BO/BOC is about 2 times higher than that of BO/BOC, suggesting the more effective separation of charge carriers over OV-BO/BOC electrode. However, the photocurrent density of R-BO/BOC obviously reduced after the repair of surface OVs. Therefore, the introduction of surface oxygen vacancy can effectively improve the charge transfer rate and electron-hole separation efficiency of the as-prepared OV-BO/BOC sample.

Moreover, the photoluminescence (PL) spectra was recorded to investigate the electron-hole pair recombination speed and the capturing electron probability [30]. Fig. 7c shows the steady-state PL spectra of the as-prepared BOC, BO/BOC, OV-BO/BOC and R-BO/BOC, respectively. The BOC exhibits a broad emission peak centered around 400–650 nm. Obvious, the OV-BO/BOC sample displays an extremely weak emission peak among all the samples, indicating a lower efficiency of photogenerated carrier recombination [23]. In addition, the emission peak at around 434 nm for R-BO/BOC is markedly enhanced due to the repair of surface-OVs. These results suggest that the OV-BO/BOC heterojunction can efficiently inhibit the direct recombination of photogenerated charge carriers. The oxygen vacancies act as catalytic centers that can capture and shed electrons to enhance the directional migration of the photo-induced carriers [18,45]. Based on these characterization results, it was speculated that the surface-OVs can capture the photo-induced electrons, inhibiting the recombination of photogenerated carriers (Fig. 7d). Subsequently, the reaction of holes with hydroxyl groups results in the formation of hydroxyl radicals. Interestingly, the photo-induced electrons can also transfer from trapped states of OVs to the surface-adsorbed oxygen, producing reactive species like $\cdot\text{O}_2^-$ and H_2O_2 (Fig. 7d) [17]. Therefore, the presence of OVs is highly favorable for the photogenerated electrons directional migration to enhance the separation efficiency.

To further investigate the charge carriers transfer characteristics among BO/BOC and OV-BO/BOC samples, DFT calculations were performed by calculating the electron density difference (EDD) of BO/BOC and OV-BO/BOC under the scenarios with and without NO absorbed on the surfaces. First, the crystal models of BO/BOC and OV-BO/BOC after geometry optimization are shown in Fig. 8a and b, respectively. The crystal structure of both perfect and defective BO/BOC indicates that the presence of oxygen vacancy can cause the larger deformation of BOC (001) lattice plane at the interface of BO/BOC, which may affect the charge carriers transfer characteristics at the interfaces. Also, the Mulliken population analysis based on the EDD results of BO/BOC and OV-BO/BOC (Fig. 8c and d) demonstrates that when oxygen vacancy is located on the BO (001) lattice plane at the interface, about 0.76 electrons transfer from BOC to BO at the heterojunction interface, but without oxygen vacancy about 0.78 electrons transfer from BO to BOC. Therefore, oxygen vacancy is served as the electron acceptor for

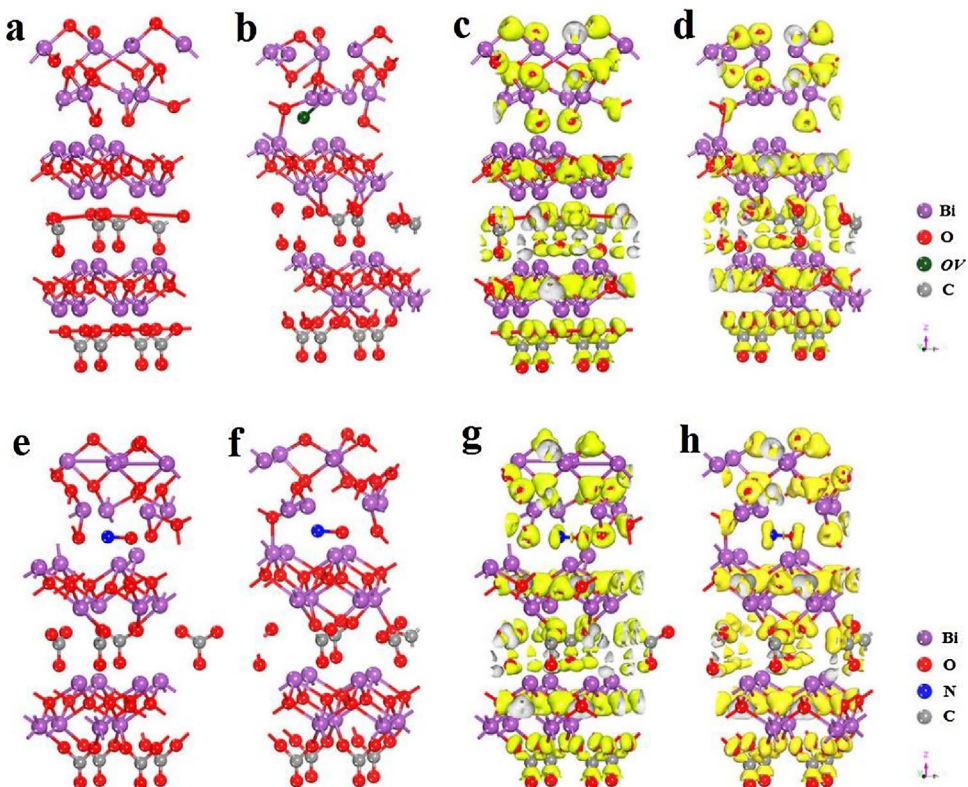
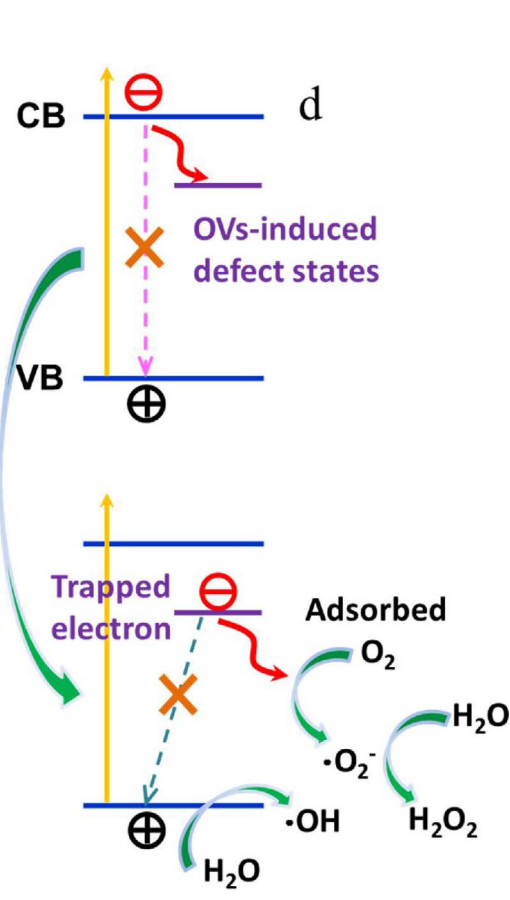
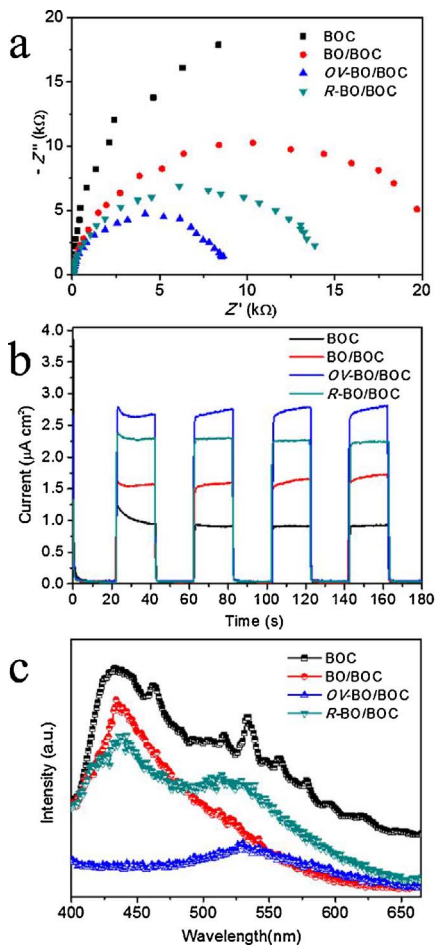


Fig. 8. The crystal models of (a) BO/BOC and (b) OV-BO/BOC after geometry optimization; The calculated electron density difference (EDD) diagrams of (c) BO/BOC and (d) OV-BO/BOC; The NO adsorption models of (e) BO/BOC and (f) OV-BO/BOC; The calculated EDD diagrams of (g) BO/BOC and (h) OV-BO/BOC with NO absorbed in the interfaces. (Notice: yellow area represents the increase of electron density). (For interpretation of the references to colour in this figure legend, the reader is referred to the web version of this article.)

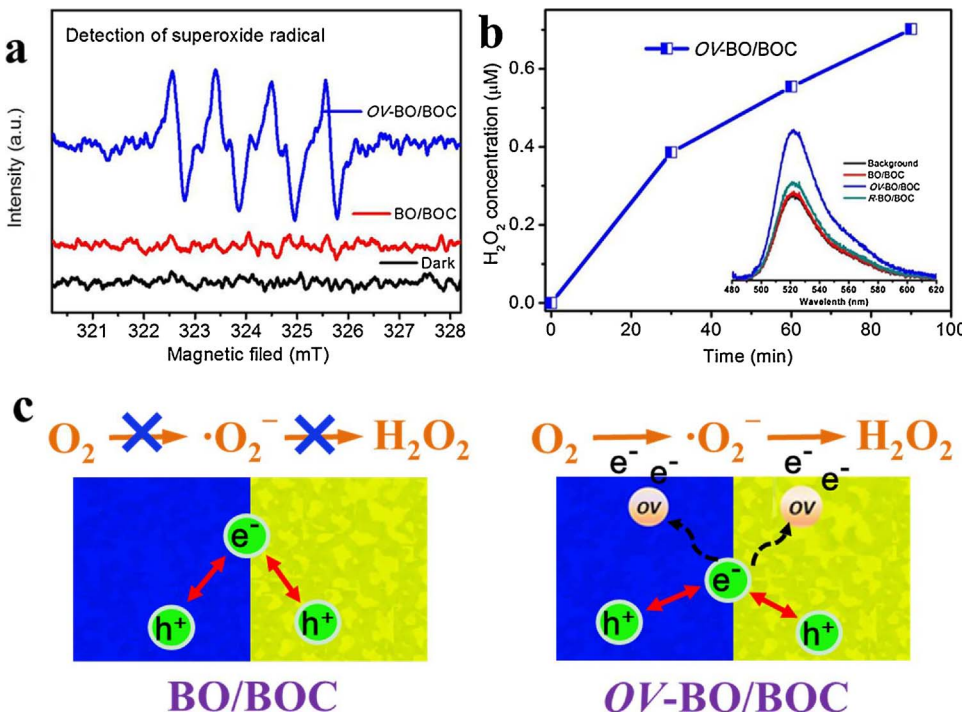


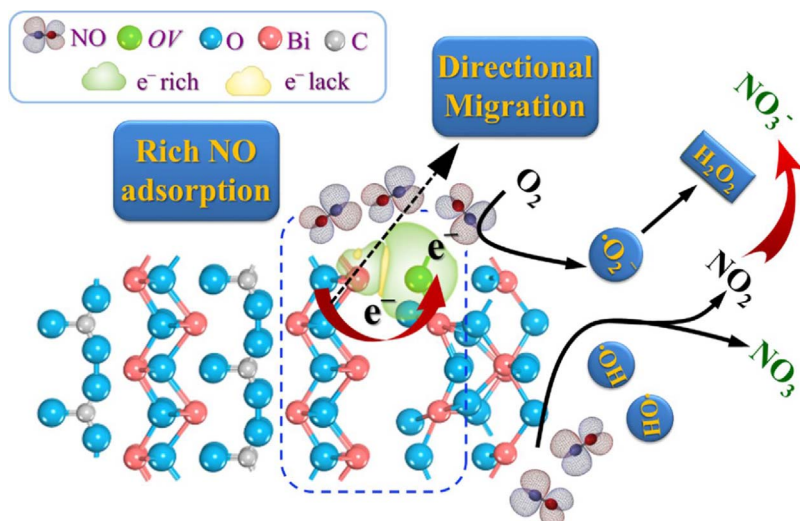
Fig. 9. The influence of oxygen vacancies on the generation of (a) $\cdot\text{O}_2^-$ and (b) H_2O_2 over BO/BOC and OV-BO/BOC samples; (c) H_2O_2 formation pathways over BO/BOC and OV-BO/BOC, respectively.

controlling the electron transfer direction. Second, the adsorption property and electron transfer characteristics between NO and the BO/BOC heterojunction interface play an important role in photocatalytic oxidation processes. Fig. 8e and f show the NO adsorption models on BO/BOC and OV-BO/BOC, respectively. The results indicate that NO physically absorbed between the heterojunction interface of BO/BOC and OV-BO/BOC. In addition, the Mulliken population analysis based on the EDD results of BO/BOC and OV-BO/BOC with NO absorbed in the interfaces (Fig. 8g and h) demonstrates that about 1.23 electrons transfer to NO in OV-BO/BOC, but only 1.07 electrons transfer to NO in BO/BOC. Therefore, the presence of oxygen defect helps to separate the photo-induced carriers at the heterojunction interface of BO/BOC and improve the photocatalytic reactivity of BO/BOC eventually.

The photocatalytic degradation reaction involves the surface reactions initiated by $\cdot\text{OH}$, $\cdot\text{O}_2^-$ and H_2O_2 to further oxidize the targeted pollutants [43,46]. The DMPO-ESR method was adopted for the direct identification of short-lived $\cdot\text{O}_2^-$ radicals during the photocatalytic removal NO over BO/BOC and OV-BO/BOC samples [47]. As shown in Fig. 9a, the signals assigned to $\cdot\text{O}_2^-$ radicals are clearly observed in OV-BO/BOC suspensions, whereas no obvious signal can be detected for the BO/BOC under identical conditions. Fig. S9 shows the intensity of $\cdot\text{OH}$ radicals over OV-BO/BOC are significantly higher than that of BO/BOC. To further determine the involvement of active species during photocatalytic reaction, the trapping experiments were performed using the scavengers, such as KI, isopropyl alcohol (IPA), potassium dichromate ($\text{K}_2\text{Cr}_2\text{O}_7$) and p-benzoquinone (PBQ) [43]. As shown in Fig. S10, once PBQ mixed, $\cdot\text{O}_2^-$ radicals are captured and the NO removal rates over the OV-BO/BOC are inhibited to 13.2% as well. Addition of PBQ clearly depresses the NO removal on OV-BO/BOC surface, but not on BO/BOC, implying the new production paths of $\cdot\text{O}_2^-$ in the OV-BO/BOC [48]. In addition, H_2O_2 production can be detected by the fluorescence analysis method [49]. As shown in Fig. 9b, the concentration of H_2O_2 in OV-BO/BOC suspension distinctly increases with extending the illumination time, while there is no H_2O_2 production in the presence of BO/BOC sample. This result demonstrates that the presence of OV-BO/BOC is essential for the photoreduction of O_2 to H_2O_2 . Moreover, the calculated EDD results of BO/BOC and OV-BO/BOC (Fig. 8c and d) illustrate that OVs can act as the electron acceptor

to control the electron transfer direction and numbers. The significant difference of DMPO- $\cdot\text{O}_2^-$ signals strongly implies that the presence of oxygen vacancies changes the transfer pathway of photoelectrons. Therefore, surface-OVs can facilitate the electron transferring from OVs to O_2 , which results in the production of $\cdot\text{O}_2^-$, and then $\cdot\text{O}_2^-$ is further reduced to H_2O_2 . The formation pathway of H_2O_2 via multistep reactions over OV-BO/BOC sample was proposed in Fig. 9c. These observations imply that H_2O_2 is essential for the conversion of NO to NO_3^- [43]. Based on these analysis, the generation of reactive species involved in the photocatalytic processes over OV-BO/BOC is much different with that of BO/BOC because of the introduction of surface oxygen vacancies, which not only guaranteed the production of more $\cdot\text{OH}$ radicals, but also provided a new route to produce $\cdot\text{O}_2^-$ radicals and H_2O_2 .

Based on the results from various characterizations and theoretical calculations, the photocatalytic mechanism of NO degradation over OV-BO/BOC was proposed (Scheme 1). Firstly, the surface oxygen vacancies on $\text{Bi}_2\text{O}_3/\text{Bi}_2\text{O}_2\text{CO}_3$ heterojunction facilitate the NO adsorption to form stable coordinate bonds, as confirmed by theoretical calculations and NO-TPD results (Figs. Figure 1 and Figure 5d). This is beneficial for the enrichment of NO at ambient concentration levels and they can increase the density of active sites, which is an important step for the sequential catalytic reactions. Secondly, a new donor level induced by the surface-OVs can effectively tune its band gap energy and enhance visible light harvesting ability, as revealed by the UV-vis DRS results. More importantly, the presence of oxygen vacancies on the surface of BO/BOC can control the electron transfer direction from BOC to BO, and can also facilitate the electron transfer between NO and BO/BOC (Fig. 8), which finally improve the charge carries separation efficiency as evidenced by photoelectrochemical tests. Finally, the introduction of surface oxygen vacancies promote the production of more $\cdot\text{OH}$ radicals and generate $\cdot\text{O}_2^-$ radicals and hydrogen peroxide. The surface-OVs can continuously capture and shed electrons to produce new active species on the defective adsorption sites, which function as the d-electron carriers that donate electrons to the anti-bonding orbital of gaseous oxygen leading to the formation of $\cdot\text{O}_2^-$ radicals [13,30]. The formed $\cdot\text{O}_2^-$ would be further transformed to H_2O_2 by capturing an electron from the oxygen vacancy, which plays the synergic roles to



deeply oxidize NO to NO_3^- [43]. From the comparative investigations above, the photocatalytic removal of NO over $\text{OV-BO}/\text{BOC}$ may involve the following reactions [50–52], Eq. (1)–(8),



Control experiments of BO/BOC and $\text{R-BO}/\text{BOC}$ were performed to investigate the significant role of oxygen vacancies in improving the photocatalytic activity. The results illustrate that the introduction of oxygen vacancy on the surface of $\text{Bi}_2\text{O}_3/\text{Bi}_2\text{O}_2\text{CO}_3$ heterojunction can facilitate the enrichment of NO with ambient concentration levels and promote the separation of photo-generated charge carriers, which leads to an excellent photocatalytic NO removal performance of $\text{Bi}_2\text{O}_3/\text{Bi}_2\text{O}_2\text{CO}_3$ heterojunction eventually.

6. Conclusion

In summary, oxygen vacancy-induced $\text{Bi}_2\text{O}_3/\text{Bi}_2\text{O}_2\text{CO}_3$ heterojunctions were prepared via an *in situ* heat treatment process, which exhibited superior gas adsorption and charge separation property compared with pristine $\text{Bi}_2\text{O}_3/\text{Bi}_2\text{O}_2\text{CO}_3$. A series of characterizations including HRTEM, Raman, and ESR confirmed the formation of surface oxygen vacancies on $\text{Bi}_2\text{O}_3/\text{Bi}_2\text{O}_2\text{CO}_3$ sample. Experimental and theoretical calculations demonstrated that the introduction of oxygen vacancy can facilitate the separation of photogenerated charge carriers which improve the photocatalytic NO removal efficiency eventually. Moreover, the presence of oxygen vacancy can facilitate the production of $\cdot\text{OH}$ radicals and $\cdot\text{O}_2^-$ radicals, which means it changed the reaction pathways for NO removal. Compared with pristine $\text{Bi}_2\text{O}_3/\text{Bi}_2\text{O}_2\text{CO}_3$ heterojunction, the $\text{OV-BO}/\text{BOC}$ performs superior photocatalytic NO removal efficiency and selectivity. This study combines the merits of surface oxygen vacancy and heterojunction, and supplies a promising strategy for the development of high efficient photocatalysts for air pollution control.

Scheme 1. Proposed schematic diagram for the migration and separation of electron–hole pairs and photocatalytic process over surface OVs-induced $\text{Bi}_2\text{O}_3/\text{Bi}_2\text{O}_2\text{CO}_3$ heterostructure photocatalyst.

Conflict of interest

None.

Acknowledgements

This research was financially supported by the National Key Research and Development Program of China (2016YFA0203000), the State Key Lab of Loess and Quaternary Geology (SKLLQGPY1605) and the National Science Foundation of China (Nos. 41401567 and 41573138). It was also partially supported by the Key Project of International Cooperation of the Chinese Academy of Sciences (GJHZ1543) and the Research Grants Council of Hong Kong (PolyU 152083/14E). Yu Huang is also supported by the “Hundred Talent Program” of the Chinese Academy of Sciences.

Appendix A. Supplementary data

Supplementary data associated with this article can be found, in the online version, at <https://doi.org/10.1016/j.apcatb.2018.01.008>.

References

- [1] J.T. Lin, M.B. McElroy, K.F. Boersma, Atmos. Chem. Phys. 10 (2010) 63–78.
- [2] R.J. Huang, Y.L. Zhang, C. Bozzetti, K.F. Ho, J.J. Cao, Y.M. Han, K.R. Daellenbach, J.G. Slowik, S.M. Platt, F. Canonaco, P. Zotter, R. Wolf, S.M. Pieber, E.A. Brun, M. Crippa, G. Ciarelli, A. Piazzalunga, M. Schwikowski, G. Abbaszade, J. Schnelle-Kreis, R. Zimmerman, Z.S. An, S. Szidat, U. Baltensperger, I. El Haddad, A.S.H. Prevot, Nature 514 (2014) 218–222.
- [3] L. Ma, J. Li, R. Ke, L. Fu, J. Phys. Chem. C 115 (2011) 7603–7612.
- [4] L. Wu, F. Li, Y. Xu, J.W. Zhang, D. Zhang, G. Li, H. Li, Appl. Catal. B Environ. 164 (2015) 217–224.
- [5] G. Li, D. Zhang, J.C. Yu, M.K.H. Leung, Environ. Sci. Technol. 44 (2010) 4276–4281.
- [6] W. Zhu, S. Xiao, D. Zhang, P. Liu, H. Zhou, W. Dai, F. Liu, H. Li, Langmuir 31 (2015) 10822–10830.
- [7] H. Gan, G. Zhang, H. Huang, J. Hazard. Mater. 250–251 (2013) 131–137.
- [8] Y. Huang, W. Wang, Q. Zhang, J.J. Cao, R.J. Huang, W. Ho, S.C. Lee, Sci. Rep. 6 (2016) 23435.
- [9] Y. Huang, W. Fan, B. Long, H. Li, F. Zhao, Z. Liu, Y. Tong, H. Ji, Appl. Catal. B Environ. 185 (2016) 68–76.
- [10] S. Ding, J. Niu, Y. Bao, L. Hu, J. Hazard. Mater. 262 (2013) 812–818.
- [11] C. Yu, W. Zhou, L. Zhu, G. Li, K. Yang, R. Jin, Appl. Catal. B Environ. 184 (2016) 1–11.
- [12] G. Li, Z. Lian, X. Li, Y. Xu, W. Wang, D. Zhang, F. Tian, H. Li, J. Mater. Chem. A 3 (2015) 3748–3756.
- [13] F. Dong, T. Xiong, Y. Sun, H. Huang, Z. Wu, J. Mater. Chem. A 3 (2015) 18466–18474.
- [14] Y. Liu, B. Wei, L. Xu, H. Gao, M. Zhang, ChemCatChem 7 (2015) 4076–4084.
- [15] X. Wu, K. Zhang, G. Zhang, S. Yin, Chem. Eng. J. 325 (2017) 59–70.
- [16] H. Li, J. Shang, Z. Ai, L. Zhang, J. Am. Chem. Soc. 137 (2015) 6393–6399.
- [17] S. Li, G. Dong, R. Haillili, L. Yang, Y. Li, F. Wang, Y. Zeng, C. Wang, Appl. Catal. B

- Environ. 190 (2016) 26–35.
- [18] D.-N. Pei, L. Gong, A.-Y. Zhang, X. Zhang, J.-J. Chen, Y. Mu, H.-Q. Yu, Nat. Commun. 6 (2015).
- [19] Y. Lv, W. Yao, R. Zong, Y. Zhu, Sci. Rep. 6 (2016) 19347.
- [20] Z. Zhao, Y. Zhou, F. Wang, K. Zhang, S. Yu, K. Cao, ACS Appl. Mater. Interfaces 7 (2015) 730–737.
- [21] W. Pipornpong, R. Wanbayor, V. Ruangpornvisuti, Appl. Surf. Sci. 257 (2011) 10322–10328.
- [22] Y.-x. Pan, C.-j. Liu, D. Mei, Q. Ge, Langmuir 26 (2010) 5551–5558.
- [23] F. Lei, Y. Sun, K. Liu, S. Gao, L. Liang, B. Pan, Y. Xie, J. Am. Chem. Soc. 136 (2014) 6826–6829.
- [24] G. Kresse, J. Furthmüller, Phys. Rev. B 54 (1996) 11169–11186.
- [25] G. Kresse, D. Joubert, Phys. Rev. B 59 (1999) 1758–1775.
- [26] J.P. Perdew, K. Burke, M. Ernzerhof, Phys. Rev. Lett. 77 (1996) 3865–3868.
- [27] P.E. Blöchl, Phys. Rev. B 50 (1994) 17953–17979.
- [28] R.S. Mulliken, J. Chem. Phys. 23 (1955) 1833–1840.
- [29] F. Wang, Z. Zhao, K. Zhang, F. Dong, Y. Zhou, CrystEngComm 17 (2015) 6098–6102.
- [30] J. Li, X. Wu, W. Pan, G. Zhang, H. Chen, Angew. Chem. 129 (2017) 1–6.
- [31] G. Zhang, X. Shen, Y. Yang, J. Phys. Chem. C 115 (2011) 7145–7152.
- [32] Y. Lee, G. He, A.J. Akey, R. Si, M. Flytzani-Stephanopoulos, I.P. Herman, J. Am. Chem. Soc. 133 (2011) 12952–12955.
- [33] S. Chen, L. Li, W. Hu, X. Huang, Q. Li, Y. Xu, Y. Zuo, G. Li, ACS Appl. Mater. Interfaces 7 (2015) 22999–23007.
- [34] X. Kong, Y. Choo, S. Chai, A. Soh, A. Mohamed, Chem. Commun. 52 (2016) 14242–14245.
- [35] Y. Lv, C. Pan, X. Ma, R. Zong, X. Bai, Y. Zhu, Appl. Catal. B Environ. 138 (2013) 26–32.
- [36] Y. Lv, Y. Zhu, Y. Zhu, J. Phys. Chem. C 117 (2013) 18520–18528.
- [37] J. In, I. Yoon, K. Seo, J. Park, J. Choo, Y. Lee, B. Kim, Chem-Eur. J. 17 (2011) 1304–1309.
- [38] H. Yen, Y. Seo, S. Kaliaguine, F. Kleitz, Angew. Chem. Int. Edit. 51 (2012) 12032–12035.
- [39] H. Lu, L. Xu, B. Wei, M. Zhang, H. Gao, W. Sun, Appl. Surf. Sci. 303 (2014) 360–366.
- [40] Y. Lv, Y. Liu, Y. Zhu, Y. Zhu, J. Mater. Chem. A 2 (2014) 1174–1182.
- [41] G. Li, B. Jiang, X. Li, Z. Lian, S. Xiao, J. Zhu, D. Zhang, H. Li, ACS Appl. Mater. Inter. 5 (2013) 7190–7197.
- [42] G. Zhang, Y. Gao, Y. Zhang, Y. Guo, Environ. Sci. Technol. 44 (2010) 6384–6389.
- [43] G. Dong, L. Yang, F. Wang, L. Zang, C. Wang, ACS Catal. 6 (2016) 6511–6519.
- [44] G. Li, L. Wu, F. Li, P. Xu, D. Zhang, H. Li, Nanoscale 5 (2013) 2118–2125.
- [45] X. Pan, M.-Q. Yang, X. Fu, N. Zhang, Y.-J. Xu, Nanoscale 5 (2013) 3601–3614.
- [46] W. Zhu, P. Liu, S. Xiao, W. Wang, D. Zhang, H. Li, Appl. Catal. B Environ. 172–173 (2015) 46–51.
- [47] F. Dong, Z. Wang, Y. Li, W.-K. Ho, S. Lee, Environ. Sci. Technol. 48 (2014) 10345–10353.
- [48] X. Ding, W. Ho, J. Shang, L. Zhang, Appl. Catal. B Environ. 182 (2016) 316–325.
- [49] L. Wang, M. Cao, Z. Ai, L. Zhang, Environ. Sci. Technol. 48 (2014) 3354–3362.
- [50] X. Wu, K. Zhang, G. Zhang, S. Yin, Chem. Eng. J. 325 (2017) 59–70.
- [51] W. Zhu, P. Liu, S. Xiao, W. Wang, D. Zhang, H. Li, Appl. Catal. B Environ. 172 (2015) 46–51.
- [52] S. Xiao, W. Zhu, P. Liu, F. Liu, W. Dai, D. Zhang, W. Chen, H. Li, Nanoscale 8 (2016) 2899–2907.